Substituted diiminoisoindoles as anticancer agents: synthesis, structural characterization, and biological evaluation

Stanislava Majerová,[a] Otakar Pojmon,[a] Filip Verunáč,[a] Lukáš Vlk,[a] Ján Vančo,[b] Veronika Nováková,[c] Zdeňka Růžičková,[a] Petr Štěpnička,[d] Zdeněk Dvořák,[e] Zdeněk Trávníček[b] and Aleš Růžička[a]*

[a] Department of General and Inorganic Chemistry, Faculty of Chemical Technology, University of Pardubice, Studentská 573, Pardubice 532 10, Czech Republic

[b] Regional Centre of Advanced Technologies and Materials, Czech Advanced Technology and Research Institute, Palacký University Olomouc, Šlechtitelů 27, Olomouc 779 00, Czech Republic

[c] Department of Pharmaceutical Chemistry, Faculty of Pharmacy in Hradec Králové, Charles University, Zborovská 2207, 50003 Hradec Králové, Czech Republic

[d] Department of Inorganic Chemistry, Faculty of Science, Charles University, Prague 128 00, Czech Republic

[e] Department of Cell Biology and Genetics, Faculty of Science, Palacký University Olomouc, Šlechtitelů 27, Olomouc 779 00, Czech Republic

Abstract

Substituted diiminoisoindoles (DIIs), **1**–**28**, were synthesized as a nitrogen-rich scaffolds for evaluation of their anticancer activity. A streamlined one-pot lithiation/isoindole formation strategy enabled the preparation of a broad portfolio of dissymmetrically substituted DIIs from substituted anilines and dicarbonitrile precursors, with nearly quantitative yields for most targets. Selected DIIs were further converted into DII–guanidine conjugates via carbodiimide-mediated guanylation. Structural characterization, including *Z*/*E* isomer distributions in solution and the solid-state, showed that isomer populations depend on electron donation from aryl substituents, while solid-state structures consistently exhibit the H-bond stabilized imino-amino/tautomeric forms. Electrochemical studies revealed irreversible oxidation and reduction processes consistent with frontier-orbital control by the iminoisoindole and guanidine/aryl substituents; computational analysis reproduced the overall trends in HOMO/LUMO energies. *In vitro* cytotoxicity was evaluated against a panel of six human cancer cell lines, including the cisplatin-resistant A2780R. Most of the DIIs showed significant-to-moderate cytotoxicity, with $IC_{50} \approx 3–33$ μM, with the best-performing di-*t*Bu sulfide-substituted compound (**13**)

on A2780R ($IC_{50} \approx 3\ \mu M$). The initial Hansch-type QSAR models, based on the lipophilicity and dipole moment descriptors, indicated that lipophilicity was the most influential parameter, with a positive coefficient indicating that greater hydrophobicity enhances biological potency, likely by improving membrane permeability or strengthening hydrophobic interactions at the target site. The QSAR models, together with the docking studies at the Sudlow I binding site, may be used as a predictive tool for the further development of DII derivatives with significant antiproliferative activities and favorable drug-like properties.

Introduction

Nitrogen-rich molecules have a plethora of functions and applications in modern biochemistry, medicinal, inorganic and organic chemistry, and technology. Applications can be sorted into areas directly related to the fundamental bioactivity of amino acids, nucleobases, enzymes, alkaloids, polyamines, porphyrins, hemes, and others. In chemical synthesis, the major area exploits their basic or superbasic properties, as evidenced by their simple use as bases or ligands in metal complexation. Two distinct types of these nitrogen-containing molecules, formally derived from carboxylic acids and carbonates, are amidines and guanidines (Figure 1). Unsubstituted amidines have been found to be selective inhibitors of trypsin-like enzymes (benzamidine) [1], anticoagulants (dabigatran) [2], antiprotozoal drugs for African trypanosomiasis and Pneumocystis pneumonia (Pentamidine) [3], or potent, reversible and competitive tyrosyl-DNA phosphodiesterase 1 (TDP-1) inhibitors (Furamidine) [4].

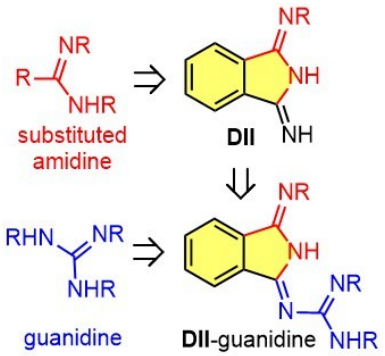

Figure 1. Virtual derivatization of **DII** systems.

Molecules of interest in this work, isoindoline 1,3-diimines (diiminoisoindoles, **DII**s), formally include two connected amidine units. Although studies of **DIIs** have often focused on the phthalocyanines derived from them, these compounds also serve as building blocks in a wide range of materials. For instance, isoindole-containing motifs appear in natural products [5] and dyes [6], and are employed in the preparation of phthalocyanine analogues (e.g., hemiporphyrazines, hydroxybenzipthalocyanines, biliazines) [7–10], BODIPY-like fluorophores (BOSHPY) [11], anion receptors [12], and electrocatalysts for oxygen evolution [13]. Notable biologically active molecules that incorporate isoindole fragments include C3a antagonists [14] and antimalarial candidates [15]. Following Linstead's discovery of unsubstituted **DII** in the 1950s, the first derivatives formed by condensation of the parent **DII** with primary alkyl and arylamines were reported [16]. In the 1970s, Siegel developed a $CaCl_2$-catalyzed condensation of phthalonitrile (a **DII** precursor) with primary arylamines to prevent phthalocyanine formation by **DII** self-condensation [17]. Later on, Ziegler, Spiessens and others reexamined the synthesis and structure of bis-1,3-(arylimino)isoindoles and bis-1,3-(alkylimino)isoindoles in both the solid state and in solution [18–20]. It was shown that bis(arylimino)isoindolines, when the aryl substituent is a coordinating base (e.g., pyridine, imidazole,

thiazole), can act as N/S tridentate, pincer-type ligands that bind a wide range of transition-metal cations [21–23]. Despite further research, heating a diiminoisindoline with an aryl amine in alcohol still represents the simplest and most widely used synthetic approach toward these compounds [24]. While this method, even if time-consuming, is useful for the preparation of symmetrical bis-1,3-(arylimino)isoindoles, the preparation of mono-aryl substituted **DII**s is usually more challenging. Generally, the synthetic methods leading to mono-aryl substituted **DII**s require long reaction times and high temperatures or catalysis, and involve tedious purification (recrystallization or chromatography) from unreacted compounds and disubstituted **DII**s, which can lead to low-to-moderate yields [25].

Recently, we reported an effective method for the preparation of monosubstituted diiminoisoindoles, and their lithium complexes by the addition of silylated lithium amides to 1,2-dicyanobenzene followed by mild protonolysis [26]. We also reinvestigated the suggested isomerization or tautomerism of substituted **DII**s in less polar solvents, where *Z* (dominant isomer)/*E*-isomerisation at the aryl-substituted nitrogen atom of the diimino tautomer takes place (Figure 2). In the solid state, the aggregation to dimers of imino-amino tautomers is present (Figure 2). According to our studies [26, 27], anilines easily add to carbodiimides upon formation of acyclic tetra- or penta-substituted guanidines, the second motif of interest with biological activity ranging from NO precursors (L-arginine) [28], antihypertensive (guanethidine) [29], AGE inhibitor (aminoguanidine) [30] to biguanides like metformin-type antidiabetic drugs [31]. Connection of **DII**s with carbodiimides is possible using the same synthetic method, when the formed guanidine is grafted on **DII**, leading to a conjugated π-electron system capable of various intra- and intermolecular interactions.

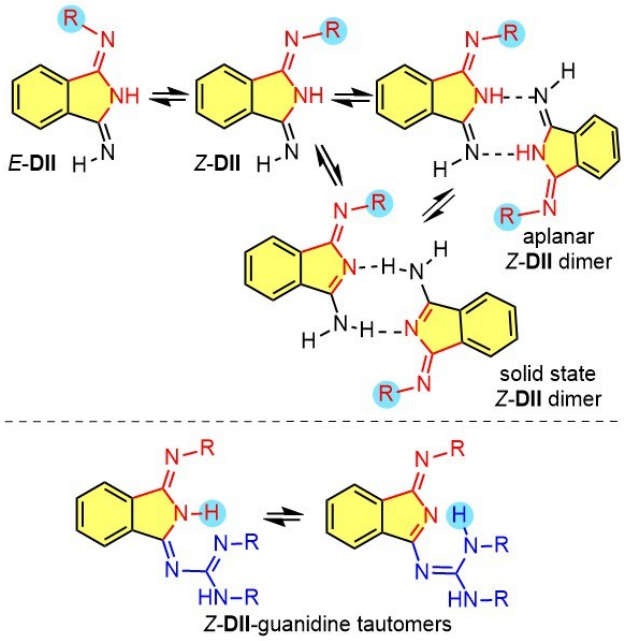

Figure 2. Plausible pathways for **DII**s isomerization in dissymmetrical systems and for **DII**-guanidines tautomerization.

To the best of our knowledge, biological profiling of substituted diiminoisoindole derivatives remains limited, although available studies demonstrate that this nitrogen-rich scaffold can yield biologically active organic molecules when appropriately substituted. Particularly relevant examples include 1,3-diiminoisoindoline carbohydrazides, which were evaluated for their *in vitro* antimalarial activity against erythrocytes infected with the chloroquine-sensitive *Plasmodium falciparum* strain NF54. The most active derivative showed an IC_{50} value of 18 nM [15]. This study also provided structure-activity relationship data and evaluated the cytotoxicity profile of organic diiminoisoindoline derivatives [15]. More recently, a few bis(pyridylimino)isoindoles were evaluated for their antioxidant, DNA cleavage, antimicrobial, microbial cell viability inhibition, biofilm inhibition, and antidiabetic activities, and were found to exhibit antibacterial activity against *E. coli*, *P. aeruginosa*, *L. pneumophila*, *E. hirae*, *E. faecalis*, and *S. aureus* with the MIC values in the 2–32 mg L^{-1} range [32]. The same compounds were also included among those displaying DNA-cleavage activity at 50 mg L^{-1} concentration and strong inhibition of microbial viability and biofilm formation at 10 mg L^{-1} [32].

In a broader medicinal-chemistry context, the isoindole family has been explored more extensively than the diiminoisoindole subclass. The parent isoindole scaffold is chemically labile and is typically encountered in stabilized, substituted, reduced or oxidized forms, including biologically relevant natural-product motifs and synthetic analogues [5]. Several isoindole-type compounds have shown promising biological properties, including anticancer activity. For example, arylthioisoindoles prepared by nucleophilic substitution within the isoindole series exhibited *in vitro* cytotoxicity against various

cancer cells, with GI_{50} values in the micromolar to submicromolar range [33]. In another study, the synthesized isoindole analogues reduced the viability of MCF-7 breast cancer and A549 lung cancer cells in a concentration- and time-dependent manner, while showing lower toxicity towards non-malignant BEAS-2B lung epithelial cells, and apoptotic morphology was also observed in treated A549 cells [34]. These findings indicate that isoindole-based organic molecules can serve as biologically relevant scaffolds. However, the direct anticancer activity of diiminoisoindole derivatives remains poorly documented, providing a clear rationale for the biological evaluation of newly prepared derivatives in cancer cell models.

Having the robust and reliable synthetic methodology at hand and targeting the use of these compounds in bioinorganic chemistry, the scope of the synthesis was evaluated, and the portfolio of compounds was expanded. Furthermore, the structures and electrochemical properties of the prepared compounds were studied, and biological activity, mainly cytotoxicity, which is important for comparison with the activities of suggested metal complexes and published phthalocyanines, was investigated.

Results and discussion

Synthesis

The optimized original synthesis [26] allows to prepare a wide range of aryl non-symmetrically substituted **DII**s straightforwardly from substituted anilines in a one-pot reaction. During the optimization, we found that the presence of a bulky trimethylsilyl group, needed for the synthesis of amidinates [35], is not necessary for isoindole formation. Therefore, it was possible to start the synthesis directly from anilines via simple first-degree deprotonation in diethyl ether at low temperature (−30 °C). Subsequently, a solution of phthalonitrile in diethyl ether was added while the reaction mixture was cooled to −50 °C. There was no need to purify the product by crystallization, which increased the overall efficiency of the reaction. Water was added directly to the reaction mixture in diethyl ether, whereupon the product precipitated and, after filtration, could be separated from inorganic salts by simple extraction. The optimized synthesis is thus more efficient, eliminating intermediate separation, saving resources (solvents and silylated molecules) and minimizing waste production. The isolated yields are nearly quantitative for **3** and **6**. The rest of the compounds were obtained in yields over 70% except for **9**, which is difficult to isolate due to its high reactivity and poor solubility. For instance, **9** underwent substitution of the fluorine atom by the methoxy group, forming **9a** during attempted crystallization from methanol.

Using the optimized method, a wide range of **DII**s and its pyrazine analogues was prepared from a variety of substituted anilines and phthalonitriles (Scheme 1 – compounds **1**-**11** and **13**) or pyrazine-2,3-dicarbonitriles (**12** and **14**), allowing the evaluation of substitutional as well as electronic effects on both aromatic parts. The current method is unsuitable for pentafluoroaniline due to lithiation issues, as well as

for nitroanilines, where the reaction results in the formation of oligomeric products and isolation of the target products is not possible.

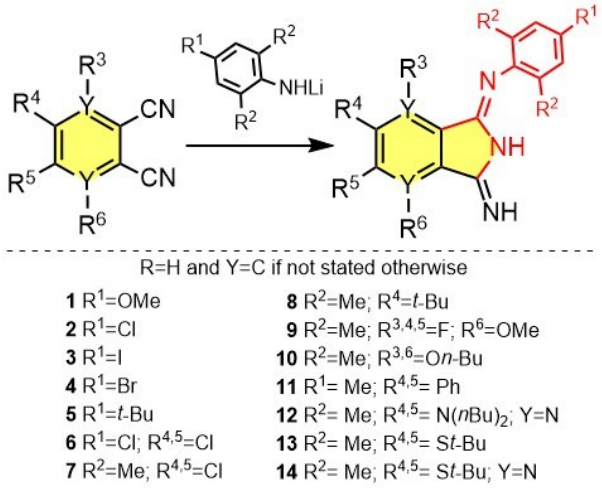

Scheme 1. Portfolio of **DII**s prepared using dissymmetrical substitution.

Furthermore, the selected **DII**s were treated with carbodiimides at 100 ˚C in toluene, producing the respective hybrid **DII**-guanidines **15**-**20** (Scheme 2) [27]. This simple method works well for all precursors, affording isolated yields that exceed 80%. However, when the reaction proceeds on air in toluene undesirable peroxide formation is observed. This can be illustrated by the structure of the **15**·BzOOH (Figure S22), resulting from the reaction of **DII**-guanidine **15** with benzyl hydroperoxide formed by solvent (toluene) oxidation. To prevent peroxide formation [36], an inert atmosphere is employed during synthesis.

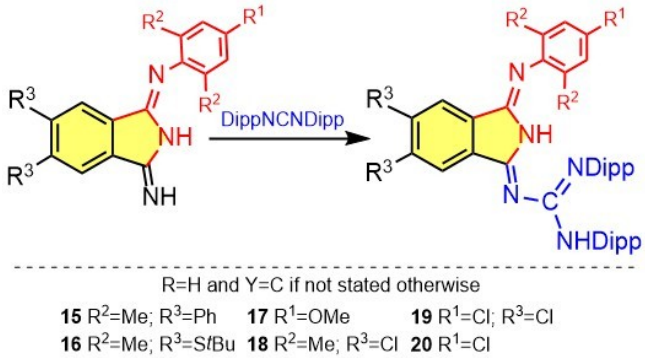

Scheme 2. Portfolio of prepared dissymmetrically substituted **DII**-guanidines (Dipp = 2,6-diisopropylphenyl).

Earlier reported [27] guanidines **21**-**28**, with similar substituents but lacking a **DII** component, were prepared for comparison of selected properties and biological activity (Scheme 3).

Scheme 3. Portfolio of reported guanidines [27] selected for comparison of biological activity.

Based on earlier work [26], one can assume that the newly prepared **DII** and **DII**-guanidine compounds to undergo the same type of *Z*/*E* isomerization as described in Figure 2. This was indeed corroborated by NMR spectroscopy by following the intensity ratios of the diagnostic atoms/groups in the ^{1}H NMR spectra recorded in THF-d8. Under such conditions, compounds **1**, **2**, **4**, **6**, **9**, **10**, **15** and **17** are present only as *Z*-isomers (for the representative ^{1}H NMR spectrum for **13** see Figure 3). Increasing electron donation from arene substituents in **5**, **7**, **8**, **11**, **16**, **18**, **19** and **20** allows the presence of *E*-isomers in 5-10%, growing to a population of ~20% for compounds **3**, **12** and **13** having substituents with even higher +*I* effect or for the pyrazine derivatives. The combination of substituent effects in **14** increases the abundance of the *E*-isomer up to 35% in the same solvent.

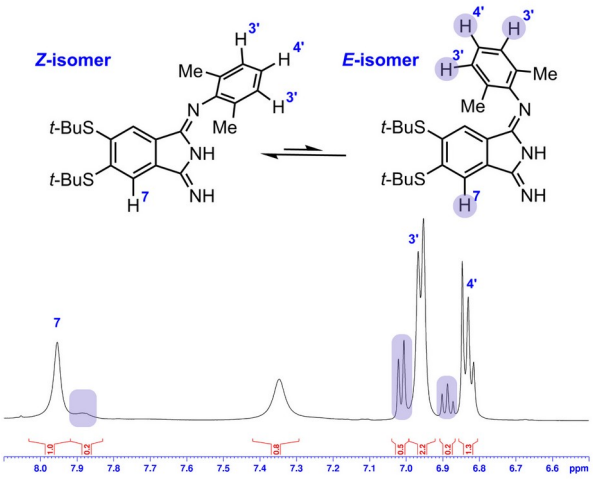

Figure 3. ^{1}H NMR spectroscopy investigation of **DII 13** isomerization (in THF-d_8).

IR spectra of selected compounds exhibited join signs supporting the presence of the isoindole and guanidine moieties (see Figs. S103-S109 in the Supporting Information). The sharp peaks near 3430 cm^{-1} are associated with hydrogen bonding, while multiple peaks centered at ca 2900 cm^{-1} are attributable

to the stretching C–H and/or N–H vibrations. The sharp and intense peaks at ca 1630 cm^{-1} can be assigned to ν(C–N) vibrations, whereas the peaks near 1530, 1050 and 810 cm^{-1} may be ascribed to the ν(C–C) skeletal vibrations of aromatic rings. Representative comparison of IR spectra of **13** and **14** (Figure S109) reveal significant differences caused by virtual replacement of phenyl for pyrazine ring within the core of the compound.

The solid-state structures of the prepared **DII**s are in line with previously published observations, in which the dimeric form of the *Z*-imino-amino tautomer (Figures 4 and 5) was observed as the most stable although the interatomic distances analysis, mainly the C2–N3 interaction, speaks for the diimino tautomer observed in solution. In compounds **9a** and **10**, an H-bond between NH and the OR substituent on the six-membered ring of isoindole is observed. The most significant difference between the compounds substituted at the *para* position of the phenyl ring (Figure 4 of **6**) and the 2,6-(dimethyl)phenyl-substituted species (example of **7**, Figure 5) is that the *para*-substituted species have the phenyl plane deviated from the orthogonal orientation by 15–45°, whereas the latter have the planes of the phenyl and isoindole rings nearly perpendicular.

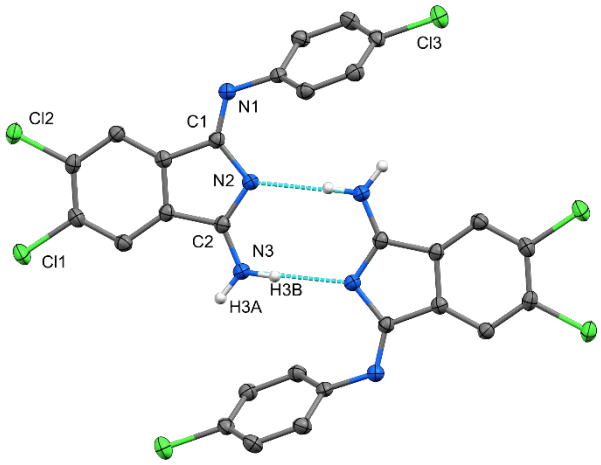

Figure 4. The ORTEP view of the molecular structure of **6** at the 50% probability level. Hydrogen atoms are omitted for clarity. Selected bond lengths (Å) and angles (°): N1–C9 1.410(2), N1–C1 1.285(2), C1–N2 1.402(2), N2–C2 1.331(2), C2–N3 1.320(2), C9–N1–C1 119.9(1), N2–C1–N1 128.6(1). Hydrogen-bond geometry (Å, °): N3—H3B···N2 2.898(2) and 175.2.

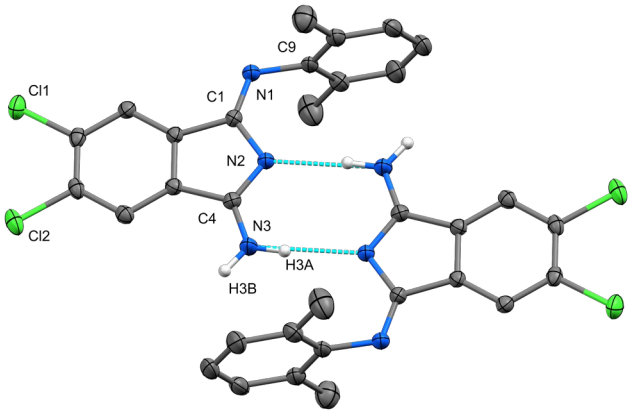

Figure 5. The ORTEP view of the molecular structure of **7** at the 30% probability level. Hydrogen atoms are omitted for clarity. Selected bond lengths (Å) and angles (°): N1–C9 1.428(3), N1–C1 1.271(3), C1–N2 1.402(3), N2–C4 1.325(3), C4–N3 1.308(3), C10–N1–C1 117.3(2), N1–C1–N2 126.5(2). Hydrogen-bond geometry (Å, °): N3—H3A···N2 2.877(3) and 174.1.

An additional stabilization factor for the dimeric structure, combining two molecules of imino-amino tautomers into dimers, in the solid state, could be found in weak interactions between N3-H3A,B and the π-system of the phenyl ring (Figures 4 and 5). Such a connection, already postulated and described [37–39] for interactions between ammonia and benzene or an N-H moiety and an aromatic ring in peptides, can bring stabilization energy up to 4 kcal/mol. In the case of **DII** species, **7** was selected as a model compound for the primary evaluation of this phenomenon. The optimized structure (starting from coordinates determined by XRD; B3LYP/def2-TZVP/CPCM-water/D3 level of theory) [40–44] was analyzed by NCI (Figure 6) [45] and AIM (Figure S32) [46] approaches. The dimer of **7** exhibits strong resonance-assisted hydrogen bonding (9.6 kcal/mol) between one of the amino group hydrogens, whereas the second is employed in the N-H…π interaction (Figure 6) of 1.6 kcal/mol.

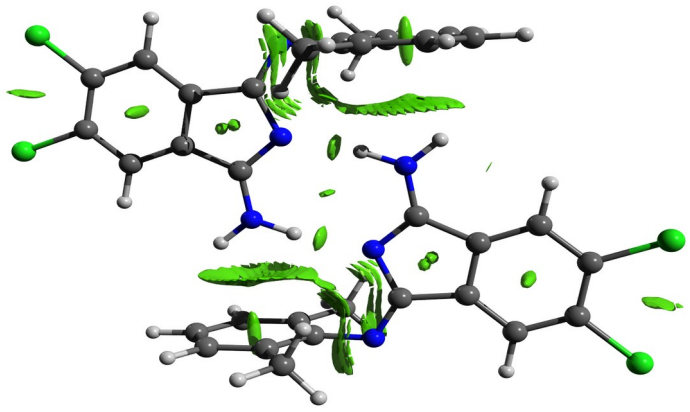

Figure 6. Representation of weak interactions within the dimer of **7**, studied *via* NCI analysis.

In contrast to the experimentally observed and theoretically approved dimeric solid-state structures with a planar arrangement of **DII** parts, our NMR investigation and theoretical calculations indicated that this

dimer of *Z*-diimino tautomers cannot exist as a planar species in solution [26], which is probably also the reason for dimers dissociation and the described isomerization of **1**–**14**.

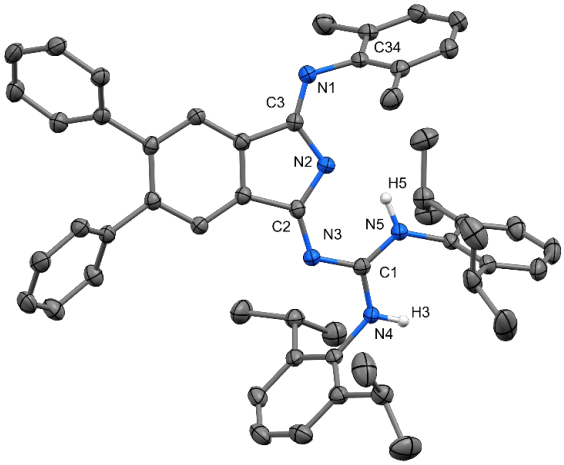

Figure 7. The ORTEP view of the molecular structure of **15** at the 50% probability level. Hydrogen atoms are omitted for clarity. Selected bond lengths (Å) and angles (°): N1–C34 1.428(2), N1–C3 1.284(2), C3–N2 1.405(1), N2–C2 1.340(2), C2–N3 1.337(2), N3–C1 1.340(2), N4–C1 1.346(2), N5–C1 1.350(2), C3–N1–C34 121.0(1), C2–N3–C1 119.8(1), N4–C1–N5 117.8(1). Hydrogen-bond geometry (Å, °): N5—H5···N2 2.601(2) and 142.3.

In hybrid **DII**-guanidines **15**-**20**, the *Z*-isomers are also observed in the solid state (Figure 7). All compounds exhibit extensive π-electron conjugation within the **DII**-guanidine moiety as well as the resonance-assisted hydrogen bonding between isoindole N2 and the hydrogen localized on N5, whereas the second hydrogen on N4 has no contact with any donor. In case of the 2,6-dimethyl phenyl-substituted species **15**, **16** and **18**, the planes of the phenyl and isoindole rings are again close to perpendicular, while in compounds **17**, **19** and **20** they deviate from planarity by 20–40°. The presence of the 2,6-(dimethyl)phenyl substituent in the molecules of **15**, **16** and **18** also causes notable displacement of the N5 atom from the plane defined by **DII** and the C3 guanidine atom, as mentioned before [26]. The solid-state structure of compound **17** is different due to the presence of water molecules, which interact via H-bonds with the N1 atom of **DII** and the N4 atom of the second molecule, forming linear chains within the structure.

Computations and electrochemistry

Electrochemical measurements

The electrochemical behavior of the prepared compounds was examined by cyclic voltammetry at a glassy carbon disc electrode in dichloromethane with 0.1 M $Bu_4N[PF_6]$ as the supporting electrolyte. The redox behavior of selected iminoisondoles **1**−**7** and **11**−**13**, and the prototypical compound **A** (see SI, Figure S33)**,** previously prepared simple 2,6-dimethylphenyl substituted **DII** [26], was similar. Within the accessible potential range, these compounds exhibited one oxidation (O1) and one reduction (R1)

step. Both processes were irreversible and associated with follow-up reactions that produced new redox-active species (Figure 8). Consequently, an additional weak reduction wave (R2) was observed after traversing O1, while a weak anodic wave (O2) appeared (alongside an additional, poorly defined oxidation) in anodic scans conducted after traversing R1. For some samples, the main oxidative wave O1 appeared broadened, most likely due to adsorption phenomena, making its peak potential less precisely measurable than the cathodic peak potential of R1. The deposition of electrochemically generated species was most evident during repeated scans, where it even influenced (in some samples) the redox response of the internal decamethylferrocene standard. For the 4-bromophenyl-substituted **DII 4**, the major anodic redox event (O1) was split into two consecutive irreversible oxidation steps (see the Supporting Information).

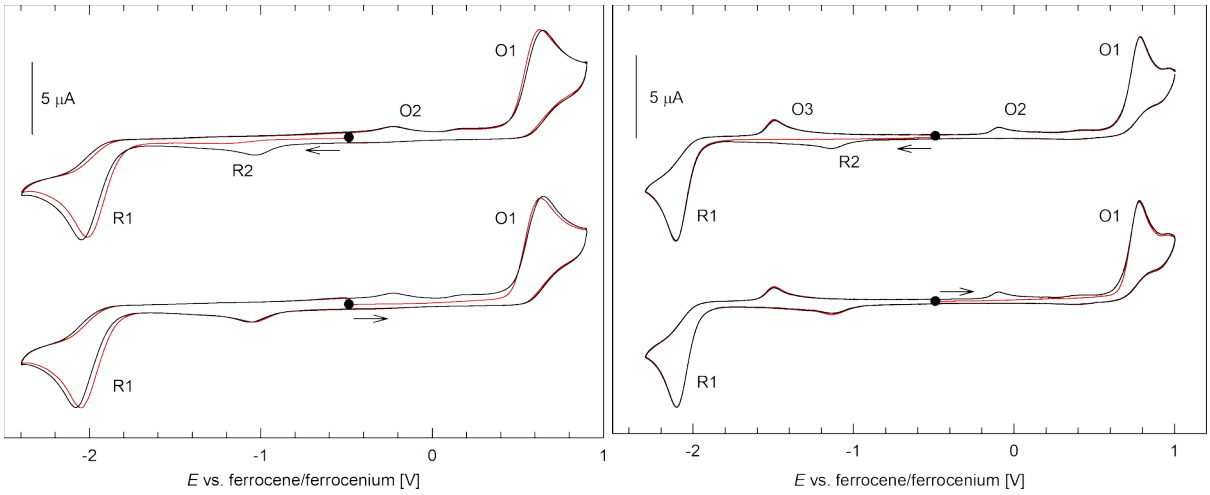

Figure 8. Cyclic voltammograms of DII **1** (left**)** and DII-guanidine **15** (right) as representative examples, recorded such that the anodic (top) or cathodic (bottom) region was investigated first. The initial scan is shown in red, the second in black; the scan direction is indicated by an arrow. The voltammograms were recorded at a glassy carbon disc electrode using samples dissolved in dichloromethane, containing 0.1 M $Bu_4N[PF_6]$ as the supporting electrolyte, and 100 mV s^{-1} scan rate.

Despite the overall similarity, the redox potentials determined for individual compounds varied (Table 1). The variation was more significant in the anodic peak potential (E_{pa}) associated with O1, which indeed corresponds with the nature of the frontier orbitals. Although extensively delocalized, the HOMO in all compounds is located predominantly on the five-membered ring and its iminoaryl substituent, whereas the LUMO is contributed mainly by the iminoisoindole fragment (Figure 8). Correspondingly, the primary electron removal leading to O1, which is expected to occur from the HOMO, is more significantly affected by the nature of the iminoaryl substituent. The primary oxidation of compound **1** bearing the electron-donating methoxy group is considerably easier than the oxidation of compounds **2** and **3** possessing the electron-withdrawing halogen substituents, and the E_{pa}(O1) values of these compounds correlated linearly with the Hammett σ_p constants (Figure S37) [47]. The structurally related

compound **6**, which carries the *t*-butyl substituent that exhibits a positive inductive effect, deviated from this trend, showing a relatively higher oxidation potential.

Introduction of the electron-withdrawing chlorine atoms onto the isoindole fragment (such as in **6** and **7**) lowered the electron density at the iminoisoindole moiety, thereby making its reduction easier, while the oxidation potential increased (*cf.* the difference in E_{pc}(R1) and E_{pa}(O1) for the pairs of compounds **2**−**6** and **A**−**7**). Conversely, compound **12**, bearing strongly electron-donating amine substituents (NBu_2) on the benzene ring, exhibited both principal redox events shifted to less positive potentials, indicating a more difficult oxidation and an easier reduction of this compound. The voltammogram of **12** displayed an additional broad and composite oxidation wave following O1 at more positive potentials (see the Supporting Information). This redox change was tentatively attributed to oxidation of redox non-innocent amine groups [48–50].

The redox behavior of the guanylated compounds **15**−**20** was generally similar to that of the parent iminoisondoles (Figure 8). In particular, the compounds exhibited an irreversible oxidation (O1) associated with follow-up processes leading to the formation of a redox-species that gives rise to additional reductive waves (R2). In the cathodic region, the compounds underwent an irreversible reduction (R1), which was associated with an anodic counterwave (O3) and an additional oxidation (O2) due to some electrochemically generated species. A wave analogous to O3 was not observed for the isoindoles. Compounds **19** differed from its analogs, showing two consecutive reductions and two narrow-spaced anodic peaks ($E_{pc} \approx -2.4$ V; see the Supporting Information). Notably, the primary reductions (R1) of **15**−**18** and **20** were observed at potentials similar to those of the corresponding isoindoles (Table 1). In contrast, oxidations O1 were consistently shifted to lower potentials (albeit in different extent), indicating a higher electron density on the isoindole fragment imparted by the electron-rich guanidine unit.

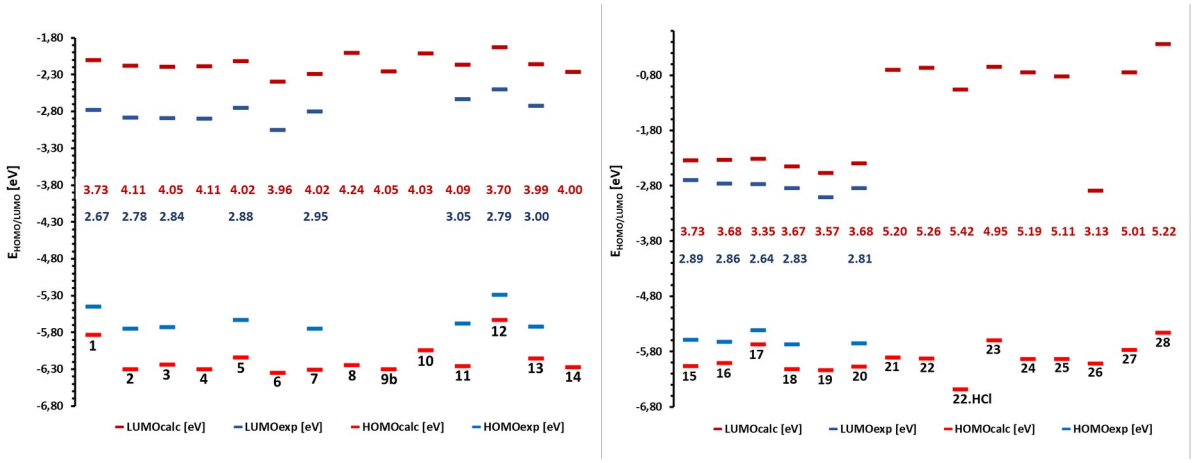

Figure 9. Comparison of the calculated energies of the HOMO and LUMO with those estimated from the differences between the first oxidation and reduction potentials.

The structures of all compounds were optimized at the B3LYP/def2-tzvp/D3 (CPCM-water) [40–44] level of theory and APT atomic charges, dipole moments and HOMO/LUMO shapes and energies were determined and visualized (see SI). In all cases, both the HOMO and LUMO are delocalized through the diiminoisoindole and guanidine parts of the molecules. As expected, dipole moment vectors are in almost all cases in the plane of **DII** and do not differ much in direction, but the values are extremely influenced by substituents (Figure S34–S36).

The electrochemically determined HOMO and LUMO energies show strong agreement with the calculated values in terms of their overall trends. However, the calculated HOMO energies are consistently about 0.3 eV lower, while the calculated LUMO energies are higher by a comparable amount relative to the experimentally observed values for both series. Despite these systematic offsets, the HOMO–LUMO gaps are similar across all compounds (Figure 9). The most nucleophilic compounds in the series are **1**, **12** and **17**, having the highest HOMO energy associated with the OMe substituent on the phenyl or bis(*n*-butylamino)-substituted pyrazine rings. The comparative series of guanidines **21**-**28** exhibits similar trends in HOMO energies governed by substituents, with the most basic **28**, substituted by methoxyphenyl as well as two cyclohexyl groups. In contrast, electrophilicity is expected to be much lower than for **1**-**20**, with the exception of 3-nitrophenyl guanidine **26**.

In vitro cytotoxicity

In vitro cytotoxicity of the studied compounds (**1**–**28**), including 11 **DII** derivatives, 9 guanidines (**1**–**13** and **21**–**28**; compounds **8** and **14** were insoluble, and fluorinated **9** was instable in the media), 6 **DII**-guanidine conjugates (**15**–**20**; Table S3), and cisplatin (CDDP) and doxorubicin (DOX) as the reference standards was evaluated against a panel of six cancer cell lines (Tables 1 and 2). In addition, the normal MRC-5 cell line was used to estimate the selectivity index (SI). The results, following the 24 h incubation, are summarized in Table 1. The obtained data revealed that the studied compounds exhibit significant-to-moderate *in vitro* cytotoxicity against most cancer cell lines, with IC_{50} values ranging from 3.2 to 45.6 μM, although IC_{50} values could not be determined in some cases due to the limited solubility of the compounds in the culture medium. Overall, compound **13** was the most promising candidate, with IC_{50} values of 3.2–11.1 μM across the series of cancer cells. Compounds **6**–**13** and **21**–**25** were found to be significantly active against A2780 and A2780R cells, with IC_{50} values of 3.2–12.3 μM, while showing moderate activity against A549, HOS, PC3 and MCF-7 cells. On the contrary, the compounds representing the guanidine-functionalized diiminoisoindoles **15**–**20** exhibited limited solubility, and thus IC_{50} values could not be determined within the concentration range used, i.e. up to 50, 25, and 10 μM.

The highest selectivity index (SI), defined as the ratio of the IC_{50} values in normal MRC-5 cells to those in A2780 cancer cells was found for compounds **11**, **12**, **21**, **22**, **22** · HCl and **24**, with the values above 5.5. Conversely, most of the compounds exhibited promising values of resistance factors (RF) ≈ 0.7–1.4, defined as the ratio of IC_{50} values in A2780R to those in A2780 cell lines, showing considerable IC_{50}

values on the cisplatin-resistant A2780R cell line, with $IC_{50} \approx 3.2–14.0$ μM, thus significantly exceeding cisplatin (RF = 2.7) and comparable with doxorubicin.

Table 1. Half-maximal inhibitory concentrations (IC_{50}, μM) of the selected compounds, and cisplatin (CDDP) and doxorubicin (DOX), used as reference standards, determined after 24 h of treatment against human cancer cell lines, including ovarian carcinoma (A2780 and cisplatin-resistant A2780R), lung adenocarcinoma (A549), osteosarcoma (HOS), prostate adenocarcinoma (PC3), and breast adenocarcinoma (MCF-7), as well as the non-tumorigenic MRC-5 fibroblast cell line. Data are reported as mean ± standard deviation.

	Cell lines								
Cpd.	**A2780**	**A2780R**	**A549**	**HOS**	**PC3**	**MCF-7**	**MRC-5**	**SI[a]**	**RF[b]**
1	31.1±3.8	43.6±2.0	>50	>50	>50	>50	>50	>1.6	1.4
2	19.9±1.2	>50	>50	>50	>50	43.2±3.6	>50	>2.5	>2.5
3	45.6±3.8	>50	>50	>50	>50	>50	>50	>1.1	>1.1
4	25.0±0.8	44.8±2.0	>50	>50	>50	45.4±3.2	>50	>2.0	1.8
5	14.8±1.1	13.3±0.4	32.6±2.6	30.4±3.4	28.2±0.7	23.2±2.0	35.1±3.8	2.4	0.9
6	10.1±0.1	7.5±1.2	16.1±2.3	14.8±0.8	24.6±1.4	14.5±3.8	20.2±2.3	2.0	0.7
7	12.2±1.9	12.3±0.8	38.9±4.2	45.1±4.2	36.7±4.2	24.7±2.6	40.7±3.8	3.3	1.0
10	7.7±0.9	10.7±1.7	16.4±3.2	17.2±0.7	15.2±2.4	23.1±2.0	23.2±2.1	3.0	1.4
11	6.5±1.1	8.1±1.4	29.7±3.6	26.3±1.8	27.7±3.8	18.6±3.8	37.2±2.3	5.7	1.2
12	7.5±0.3	7.8±0.9	>10	>10	>10	>10	>10	>6.7	1.0
13	4.3±0.9	3.2±0.7	10.9±1.1	11.1± 0.9	10.1±0.8	10.0±0.8	11.0±1.0	2.5	0.7
21	7.7±1.1	10.2±0.7	19.6±2.1	29.2±2.8	32.9±1.4	28.8±0.8	>50	>6.5	1.3
22	7.1±1.0	6.3±1.0	17.3±1.6	22.0±3.4	31.5±0.5	>50	>50	>7.0	0.9
22·HCl	6.7±0.7	8.1±1.4	17.5±3.0	20.4±4.5	19.0±1.6	27.8±0.7	>50	>7.5	1.2
23	8.2±0.3	11.5±0.4	23.2±2.7	37.4±2.0	33.5±3.6	27.0±3.4	40.0±1.6	4.9	1.4
24	9.1±1.7	12.8±1.3	19.7±1.0	21.4±1.5	26.4±2.7	42.1±4.5	>50	>5.5	1.4
25	15.5±0.6	14.0±1.3	29.7±3.6	26.3±1.8	27.7±3.8	>50	>50	>3.2	0.9
26	18.9±3.4	28.0±2.0	42.0±4.0	29.0±3.9	27.1±2.2	31.5±3.8	>50	>2.6	1.5
27	>50	>50	>50	>50	>50	>50	>50	>1	>1
28	>41	>50	>50	>50	>50	>50	>50	>1.2	>1.2
CDDP	15.6±1.3	42.1±0.6	>50	44.2±2.3	>50	17.3±1.7	>50	3.2	2.7
DOX	2.9±0.8	3.6±0.2	>20	9.1±3.9	>20	5.1±3.4	>20	6.9	1.2

Note: The maximum concentration of the corresponding compound used in the experiments was 50 μM, except for compound **12**, owing to its limited solubility in the culture medium. In the case that the IC_{50} value could not be determined within the concentration range used, it is reported as >50, >20, and >10, respectively. [a,b] The value of the selectivity index (SI) was calculated as the ratio of the IC_{50} values in normal MRC-5 cells to those in A2780 cancer cells, while the resistance factor (RF) was calculated as the ratio of IC_{50} values in A2780R to those in A2780 cell lines. Cpd. = compound.

To shed light on the dynamics of the antiproliferative effect of the studied complexes, five candidates (compounds **1**, **5**, **6**, **10** and **11**) were selected for time-dependent experiments in A2780 cells over the 24–72 h period. The obtained results are presented in Table 2. The data revealed that time has an insignificant effect on the *in vitro* cytotoxicity of the compounds, as the IC_{50} values remain nearly unchanged over time. This conclusion contrasts with that for cisplatin (CDDP) and doxorubicin (DOX), where the IC_{50} values decrease markedly with increasing time.

Table 2. The time-dependent cytotoxic effects (24–72 h) of the selected compounds, cisplatin (CDDP) and doxorubicin (DOX), toward A2780 ovarian cancer cells are presented as IC_{50} values (μM) ± standard deviation.

Compound	24 h	48 h	72 h
1	34.8±2.4	29.4±2.1	36.6±3.0
5	16.0±0.8	19.1±0.6	15.5±0.9
6	10.0±0.3	9.6±0.2	10.6±0.4
10	6.9±0.7	7.0±1.4	8.8±1.9
11	6.7±1.4	5.4±0.7	5.0±1.7
CDDP	12.5±1.0	2.7±0.5	1.94±0.09
DOX	2.9±0.8	0.2±0.1	0.2±0.05

QSAR analysis – initial models

The classical Hansch-type QSAR models were suggested and further investigated using multiple linear regression to relate lipophilicity (log P), electronic (dipole moment, DM) descriptors, and steric descriptors (molar refractivity, MR) to biological activity (the decadic logarithm of the $1/IC_{50}$ concentration obtained in the MTT test for the most susceptible cell line A2780). The resulting four-parameter model, however, suffered from several methodological flaws stemming from overparameterization and collinearity between the log P and MR descriptors. Therefore, reduced/minimal QSAR models were suggested using the combination of log P+DM descriptors (the log P+DM model) and the log P descriptor only (also referred to as the log P model).

The logP+DM model was based on the equation $\log(1/IC_{50}) = (4.133 \pm 0.277) + (0.1075 \pm 0.0279)\times\log P + (0.0253 \pm 0.0234)\times DM$ and exhibited marginal qualitative parameters, i.e. goodness-of-fit $R^2=0.598$, and acceptable statistical significance $F(2,10)=7.45$, $p=0.01044$, SEE = 0.176 and MAE = 0.119.

The log P model was based on the equation $\log(1/IC_{50})=(4.3405 \pm 0.1776)+(0.10156 \pm 0.02859)\times\log P$ with $R^2=0.534$. The model showed improved statistical significance, with $F(1,11)=12.62$, $p=0.00453$, SEE = 0.184 and MAE = 0.138

Based on the above-mentioned parameters describing the goodness-of-fit and robustness of the QSAR models, we can conclude that both models satisfy only some of the four principal criteria in accordance with the OECD guidelines and should therefore be treated as incomplete, as for the number of the training data, and at this stage, imperfect [51]. For more detailed numerical outputs, please refer to the Supporting Information, section Details regarding the suggested QSAR models. In both models, lipophilicity emerged as the most influential parameter, with a positive coefficient indicating that greater hydrophobicity enhances biological potency, likely by improving membrane permeability or strengthening hydrophobic interactions at the target site. The contribution of the dipole moment was not significant ($p \approx 0.307$). Model robustness was described by LOO cross-validation ($Q^2_{LOO} = 0.44$ for the logP+DM model and $Q^2_{LOO} = 0.41$ for the log P model), while external predictivity was evaluated using a training set of 13 compounds and a random testing set of 4 compounds with $Q^2ext = 0.43$ for the log P+DM model and $Q^2ext = 0.51$, indicating the improved external predictability of the log P model. The relatively small difference between R^2 and Q^2_{LOO} suggests minimal overfitting despite the limited dataset size. Y-randomization testing further excluded chance correlation, as evidenced by a higher cR^2p^2 value (0.53 for the log P+DM model and 0.49 for the log P model). Applicability domain analysis using leverage statistics revealed no influential outliers in both QSAR models, supporting the reliability of model predictions within the defined chemical space (for further details and the Williams plots, see the Supporting Information).

Overall, the proposed QSAR models meet some of the established validation criteria and provide valuable insight into the structural requirements governing biological activity. They can therefore serve as a suitable initial predictive model for the further development of new DII derivatives with significant antiproliferative properties.

Docking analysis

The binding of drugs to human serum albumin (HSA) significantly influences their pharmacokinetics and biological availability. Consequently, we aimed to predict how compounds **1**–**28** bind to the Sudlow I site, which is a common binding site for many semipolar drugs.

In general, the molecular docking of the ligands **1**–**28** to the Sudlow I binding site of HSA revealed two main types of binding patterns within this binding site. The first type primarily represents the hydrophobic interaction pattern deep within the interior of the Sudlow I site (see Figure 10 for compound **13**), characterized by hydrophobic and π-stacking interactions between the main skeletons of molecules **1**–**14** and **28** (except for **11**, which has a bulkier molecule). Compounds **7**-**14** were able to form hydrogen bonds between the polar parts of their molecules (e.g., imine and heterocyclic nitrogen atoms) and the suitable side-chains of amino acids in the polar part of the Sudlow I binding site, e.g. Arg218, Ala291, Lys199, Arg257, Glu188, Glu153, or His242. The second type of binding pattern represents the bulkier and more branched dissymmetrically substituted **DII**-guanidines **15**-**20** and differently substituted

guanidine derivatives **21**-**27** occupied the shallower parts of the Sudlow I binding site, forming a wide set of hydrophobic interactions and hydrogen bonds with the side-chains of the amino acids Lys436, Arg218, Arg160, Arg222, Asp451, Lys195, Asp295, and Tyr452 (see an example for compound **20** in Figure 11 and for compound **22** in Figure 12). The detailed information regarding the docking of the compounds **1**–**28** (except for **13**, **20**, and **22**) into HSA, together with hyperlinks to raw data and Ligplot+ results, are given in Figures S38–S62 in the Supporting Information.

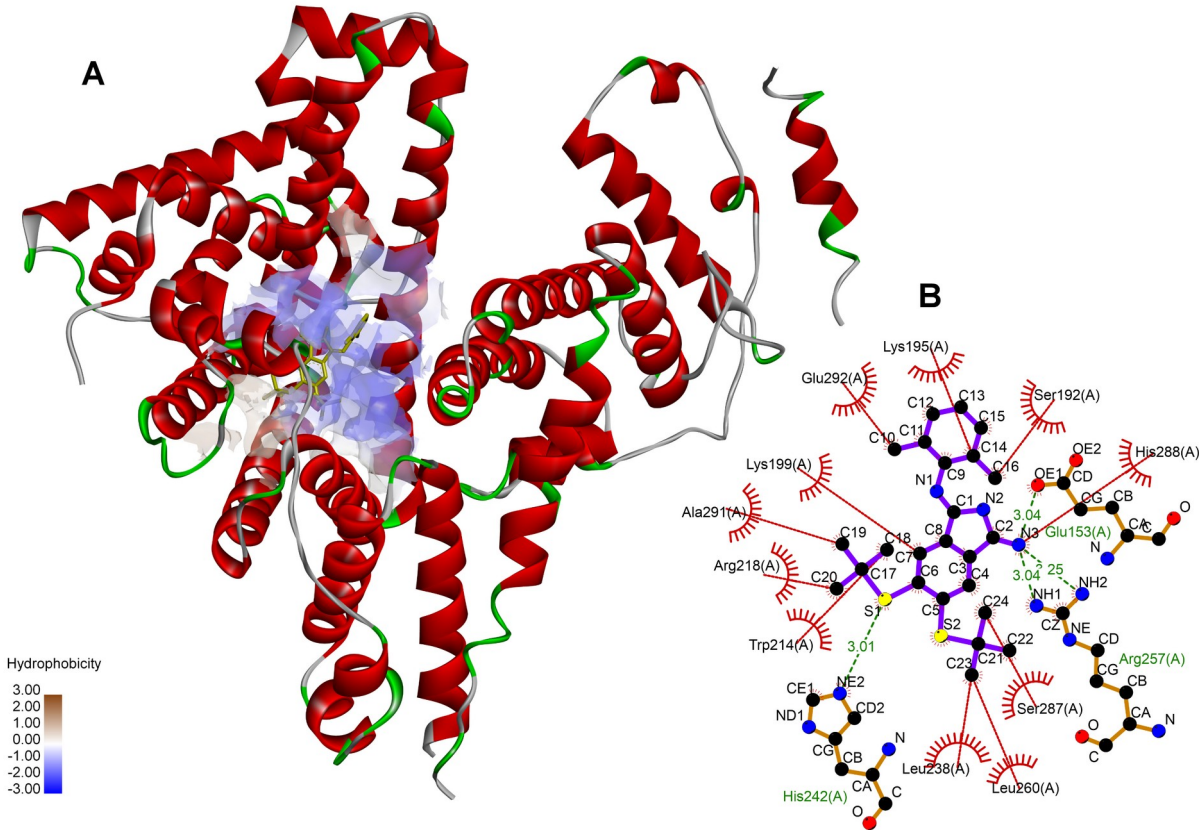

Figure 10. The position of the docked compound **13** (**A**) deep within the Sudlow I binding site of HSA, stabilized by numerous hydrophobic interactions and π-stacking interactions and several hydrogen bonds with the side chains of amino acids Glu153, Arg257, and His242 (*green dashed lines, showing the donor-acceptor distance in Å*). The surface in part **A** represents the solvent-accessible surface coloured by the hydrophobic character of the parts of the HSA protein residues within a 5 Å radius from the docked molecule (relative, on a scale from brown to blue). The graphics were created using Biovia Discovery Studio Visualizer, ver. 19.1.0.18287 (Dassault Systemes Biovia Corporation, 2018) and LigPlot+, ver. 2.3.1 [52].

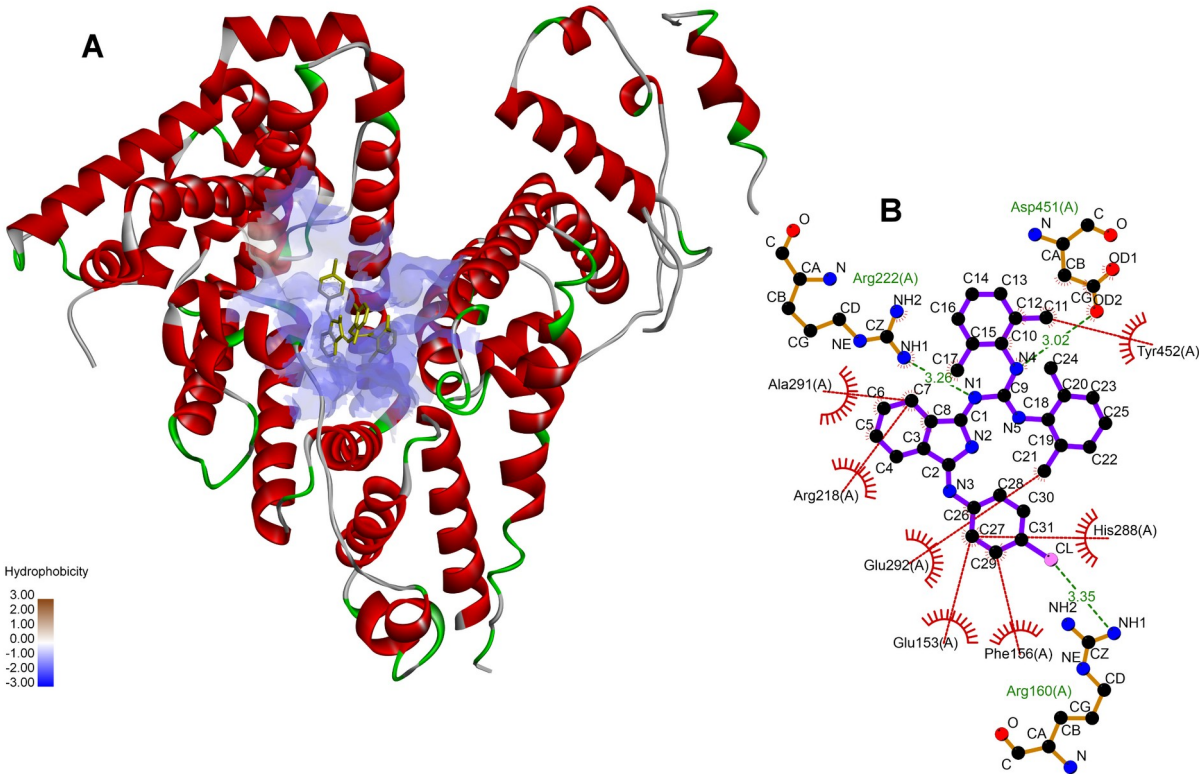

Figure 11. The position of the docked compound **20** (**A**) in the shallower regions of the Sudlow I binding site of HSA, stabilized by numerous hydrophobic interactions and π-stacking interactions and several hydrogen bonds with the side chains of amino acids Arg222, Asp451, and Arg160 (*green dashed lines, showing the donor-acceptor distance in Å*). The surface in part **A** represents the solvent-accessible surface coloured by the hydrophobic character of the parts of the HSA protein residues within a 5 Å radius from the docked molecule (relative, on a scale from brown to blue). The graphics were created using Biovia Discovery Studio Visualizer, ver. 19.1.0.18287 (Dassault Systemes Biovia Corporation, 2018) and LigPlot+, ver. 2.3.1 [52].

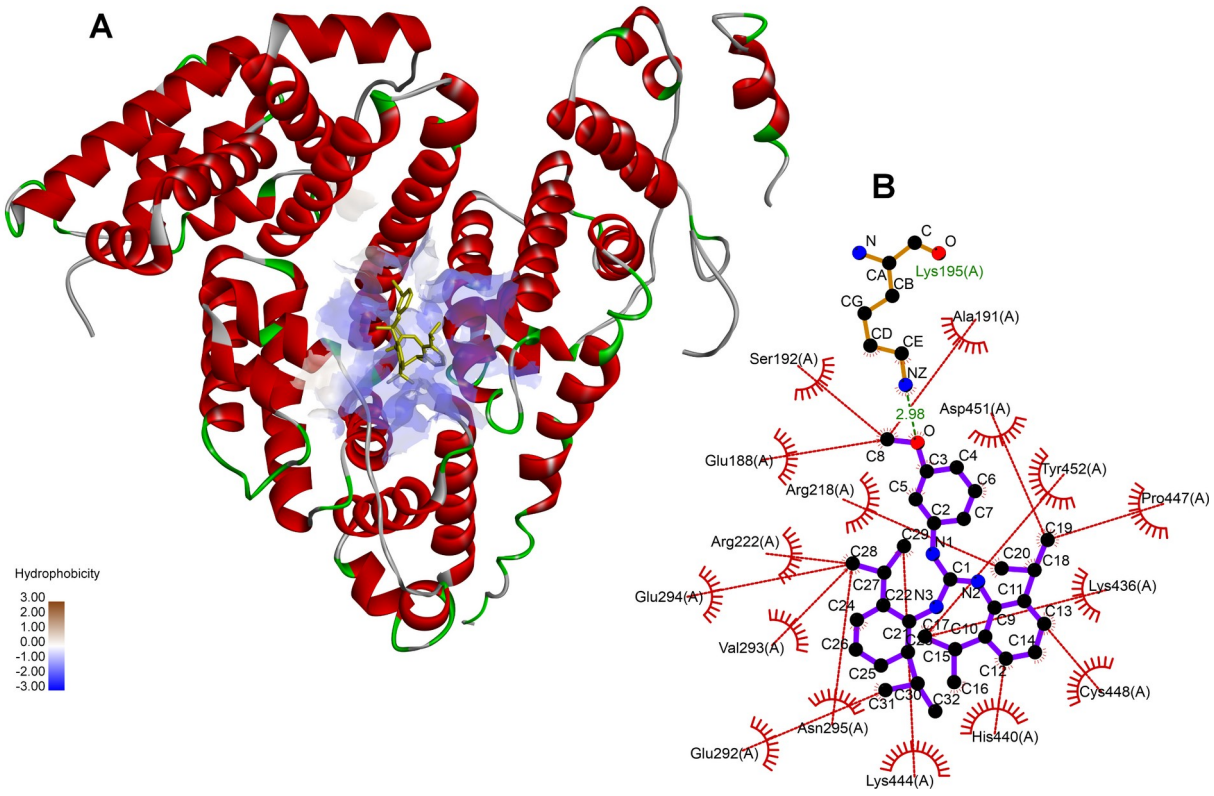

Figure 12. The position of the docked compound **22** (**A**) in the shallower regions of the Sudlow I binding site of HSA, stabilized by numerous hydrophobic interactions and π-stacking interactions and forming a hydrogen bond with the side chain of Lys195 (*green dashed lines, showing the donor-acceptor distance in Å*). The surface in part **A** represents the solvent-accessible surface coloured by the hydrophobic character of the parts of the HSA protein residues within a 5 Å radius from the docked molecule (relative, on a scale from brown to blue). The graphics were created using Biovia Discovery Studio Visualizer, ver. 19.1.0.18287 (Dassault Systemes Biovia Corporation, 2018) and LigPlot+, ver. 2.3.1 [52].

The docking procedure also provided predicted binding energies (Table 3), which may serve as comparative indicators of the relative affinity of compounds **1**–**28** and the reference drugs (*S*)-warfarin and phenylbutazone for the Sudlow I binding site of HSA. The binding energies of warfarin (−7.305 kcal/mol) and phenylbutazone (−7.399 kcal/mol) confirm that the known Sudlow I binders produce binding energies in the same range as the most active DII derivatives, supporting the biological relevance of the docking predictions and the potential interactions of the DII derivatives with lower binding energies compared with warfarin and phenylbutazone, as well as their absorption and distribution profiles. In combination with the predicted binding modes and protein–ligand interaction patterns, these results provide a structural basis for estimating the potential extent and mode of HSA binding of the investigated compounds. Since HSA binding can substantially influence the free fraction, distribution, transport, clearance, and overall pharmacokinetic behavior of drugs, in silico assessment of HSA interactions may provide useful information during early drug discovery and lead optimization [53].

Thus, the present docking analysis may help anticipate differences in the serum protein-binding behavior of the DII derivatives and identify compounds warranting further experimental evaluation of HSA binding and drug-like properties.

Table 3. The binding energies of compounds **1**–**28** to the Sudlow I binding site of HSA, as calculated using the AutodockVina algorithm with the SwissDock tool.

Compound	**Binding energy Sudlow I** (kcal/mol)	**Compound**	**Binding energy Sudlow I** (kcal/mol)
1	-8.916	**15**	-10.083
2	-8.996	**16**	-8.381
3	-8.900	**17**	-8.536
4	-8.969	**18**	-8.831
5	-9.285	**19**	-9.311
6	-8.731	**20**	-8.834
7	-7.936	**21**	-5.701
8	-11.223	**22**	-6.177
9	-8.311	**23**	-5.867
10	-8.135	**24**	-5.558
11	-9.138	**25**	-6.273
12	-7.302	**26**	-6.174
13	-8.339	**27**	-6.610
14	-8.294	**28**	-8.197
warfarin	-7.305	**phenylbutazone**	-7.399

Conclusions

A simplified one-pot synthetic method afforded a wide variety of dissymmetrically substituted DIIs in high yields, and the subsequent carbodiimide-mediated guanylation produced **DII**–guanidines (**15**–**20**) efficiently, provided the reactions were performed under an inert atmosphere to suppress peroxide formation. A solution NMR study revealed that the proportion of the less populated *E* isomer increases with the electron-donating ability of the substituents (and grows further for strongly donating or pyridazine/pyrazine-type substituents), while the solid-state structures remained consistent with stabilized imino-amino/*Z*-derived motifs and extensive intra-/intermolecular interactions. The primary redox steps occur at the iminoisoindole core, and their redox potentials are modulated by the aryl and guanidine substituents. DFT calculations reproduced trends in HOMO/LUMO energies for both **DIIs** and **DII**–guanidines (despite systematic energy offsets), with HOMO–LUMO gaps remaining broadly similar across compounds.

The **DII**s displayed significant-to-moderate in vitro cytotoxicity against most of the cancer cell lines tested (IC_{50} values roughly in the low-to-mid μM range), with compound **13** exhibiting the best antiproliferative properties (IC_{50} = 3.2–11.1 μM). Many guanidine-functionalized conjugates showed limited measurable cytotoxicity, primarily due to solubility constraints under the assay conditions,

preventing definitive activity ranking for **15**–**20**. Time-dependent experiments (24–72 h) indicated that the tested **DII**s' cytotoxic effects change only slightly over time, in contrast to the stronger time-dependence observed for cisplatin and doxorubicin. Several compounds also showed promising profiles in the cisplatin-resistant A2780R line (with resistance factor values suggesting retained potency for multiple **DII**s).

Two initial Hansch-type QSAR models, the first one based on the combination of log P and dipole moment, while the second one, a parsimonious model based on log P molecular descriptor alone, linked activity to lipophilicity as the most significant descriptor relevant to antiproliferative activity against the A2780 cells. Docking to human serum albumin predicted plausible Sudlow I binding modes via hydrophobic contacts and hydrogen bonding, consistent with the idea that physicochemical properties influencing protein association may be relevant to biological performance. Docking studies revealed two principal binding modes of the DII derivatives within the Sudlow I site of HSA, depending mainly on molecular size, branching, hydrophobicity, and the positioning of polar groups. Less bulky derivatives preferentially occupied the deeper hydrophobic region of the binding pocket, whereas bulkier and more branched guanidine derivatives favored shallower regions stabilized by complementary hydrophobic and hydrogen-bonding interactions. The predicted binding energies and interaction patterns support the ability of these compounds to bind HSA and provide useful structural insight into their potential serum protein binding and pharmacokinetic behavior.

The work establishes guanidine-functionalized DIIs as a viable anticancer scaffold, pinpoints compound **13** as the most promising candidate under the tested conditions, and provides a coherent framework connecting synthesis, redox/electronic properties, key physicochemical descriptors, and cytotoxic outcomes.

Acknowledgements

Mgr. Eva Danková and Dr. Peter Šramel are thanked for the synthetic assistance and NMR measurements.

Marta Rešová (Palacký University Olomouc) for assistance with *in vitro* cytotoxicity testing.

This work was supported by the Czech Science Foundation grant no. 25-17424S and the Programme Johannes Amos Comenius under the Ministry of Education, Youth and Sports of the Czech Republic [No. CZ.02.01.01/00/23_021/0008593], and the Charles University Research Centre program (project no. UNCE/24/SCI/010).

Veronika Nováková would like to thank the project New Technologies for Translational Research in Pharmaceutical Sciences /NETPHARM (project ID CZ.02.01.01/00/22_008/0004607), co-funded by European Union.

References

1. Stürzebecher, J.; Vieweg, H.; Wikström, P.; Turk, D.; Bode, W. Interactions of thrombin with benzamidine-based inhibitors. *Biological Chemistry Hoppe-Seyler* **1992**, *373*(2), 491–496. https://doi.org/10.1515/bchm3.1992.373.2.491.
2. Munoz-Corcuera, M.; Ramirez-Martinez-Acitores, L.; Lopez-Pintor, R. M.; Casanas-Gil, E.; Hernandez-Vallejo, G. Dabigatran: A new oral anticoagulant. Guidelines to follow in oral surgery procedures. A systematic review of the literature. *Medicina Oral Patología Oral y Cirugia Bucal* **2016**, 0-0. doi:10.4317/medoral.21202.
3. Girard, P. M.; Brun-Pascaud, M.; Farinotti, R.; Tamisier, L.; Kernbaum, S. Pentamidine aerosol in prophylaxis and treatment of murine Pneumocystis carinii pneumonia. *Antimicrobial Agents and Chemotherapy* **1987**, *31*(7), 978-981. doi:10.1128/aac.31.7.978.
4. Huang, S. -yin N.; Pommier, Y.; Marchand, C. Tyrosyl-DNA Phosphodiesterase 1 (Tdp1) inhibitors. *Expert Opinion on Therapeutic Patents* **2011**, *21*(9), 1285-1292. doi:10.1517/13543776.2011.604314.
5. Speck, K.; Magauer, T. The chemistry of isoindole natural products. *Beilstein Journal of Organic Chemistry* **2013**, *9*, 2048-2078. doi:10.3762/bjoc.9.243.
6. Radtke, V.; Erk, P.; Sens, B. Isoindoline Pigments. *High Performance Pigments* **2009**, 221-241. doi:10.1002/9783527626915.ch14.
7. Schrage, B. R.; Nemykin, V. N.; Ziegler, C. J. Biliazine: a ring open phthalocyanine analog with aimeso/ihydrogen bond. *Chemical Communications* **2020**, *56*(49), 6628-6631. doi:10.1039/d0cc03060k.
8. Costa, R.; Schick, A. J.; Paul, N. B.; Durfee, W. S.; Ziegler, C. J. Hydroxybenziphthalocyanines: non-aromatic phthalocyanine analogues that exhibit strong UV-visible absorptions. *New Journal of Chemistry* **2011**, *35*(4), 794. doi:10.1039/c0nj00500b.
9. Muranaka, A.; Ohira, S.; Hashizume, D.; Koshino, H.; Kyotani, F.; Hirayama, M.; et al. [18]/[20]π Hemiporphyrazine: A Redox-Switchable Near-Infrared Dye. *Journal of the American Chemical Society* **2011**, *134*(1), 190-193. doi:10.1021/ja210410c.
10. Barone, N.; Costa, R.; Sripothangnok, S.; Ziegler, C. J. Dihydroxy- and Tetrahydroxydicarbahemiporphyrazine: Phthalocyanine analogues with phenol and resorcinol units. *European Journal of Inorganic Chemistry* **2010**, *2010*(5), 775-780. doi:10.1002/ejic.200900921.
11. Schrage, B. R.; Nemykin, V. N.; Ziegler, C. J. BOSHPY Fluorophores: BODIPY analogues with single atom controlled aggregation. *Organic Letters* **2021**, *23*(13), 5246-5250. doi:10.1021/acs.orglett.1c01776.
12. Dydio, P.; Zieliński, T.; Jurczak, J. Bishydrazide derivatives of isoindoline as simple anion receptors. *The Journal of Organic Chemistry* **2009**, *74*(4), 1525-1530. doi:10.1021/jo802288u.
13. Benkó, T.; Lukács, D.; Frey, K.; Németh, M.; Móricz, M. M.; Liu, D.; et al. Redox-inactive metal single-site molecular complexes: a new generation of electrocatalysts for oxygen evolution? *Catalysis Science & Technology* **2021**, *11*(19), 6411-6424. doi:10.1039/d1cy01087e.

14. Grant, E. B.; Guiadeen, D.; Singer, M.; Argentieri, D.; Hlasta, D. J.; Wachter, M. Design, synthesis, and biological activity of diiminoisoindolines as complement component 3a antagonists. *Bioorganic & Medicinal Chemistry Letters* **2001**, *11*(21), 2817-2820. doi:10.1016/s0960-894x(01)00522-4.
15. Mombelli, P.; Witschel, M. C.; van Zijl, A. W.; Geist, J. G.; Rottmann, M.; Freymond, C.; et al. Identification of 1,3-diiminoisoindoline carbohydrazides as potential antimalarial candidates. *ChemMedChem* **2011**, *7*(1), 151-158. doi:10.1002/cmdc.201100441.
16. Clark, P. F.; Elvidge, J. A.; Linstead, R. P. 722. Heterocyclic imines and amines. Part II. Derivatives of isoindoline and isoindolenine. *Journal of the Chemical Society (Resumed)* **1953**, 3593. doi:10.1039/jr9530003593.
17. Siegl, W. O. Metal ion activation of nitriles. Syntheses of 1,3-bis(arylimino)isoindolines. *The Journal of Organic Chemistry* **1977**, *42*(11), 1872-1878. doi:10.1021/jo00431a011.
18. Spiessens, L. I.; Anteunis, M. J. O. NMR Studies on imidines. V. ^{1}H and ^{13}C nuclear magnetic resonance study of the tautomerism and geometrical isomerism of 1,3-bis(arylimino)isoindolines. *Bulletin des Sociétés Chimiques Belges* **1984**, *93*(3), 205-222. doi:10.1002/bscb.19840930306.
19. Spiessens, L. I.; Anteunis, M. J. O. NMR studies on imidines. VII. The tautomerism of mono-n-aryl substituted phthalic imidines. A ^{1}H and ^{13}C nuclear magnetic resonance study. *Bulletin des Sociétés Chimiques Belges* **1988**, *97*(6), 431-452. doi:10.1002/bscb.19880970604.
20. Tamgho, I. -S.; Engle, J. T.; Ziegler, C. J. The syntheses and structures of bis(alkylimino)isoindolines. *Tetrahedron Letters* **2013**, *54*(45), 6114-6117. doi:10.1016/j.tetlet.2013.08.134.
21. Camerano, J. A.; Sämann, C.; Wadepohl, H.; Gade, L. H. Bis(pyridylimino)isoindolato−iridium complexes as epoxidation catalysts for alkenes. *Organometallics* **2011**, *30*(3), 379-382. doi:10.1021/om1010116.
22. Sauer, D. C.; Kruck, M.; Wadepohl, H.; Enders, M.; Gade, L. H. Spin density distribution in iron(II) and cobalt(II) alkyl complexes containing 1,3-bis(2-pyridylimino)isoindolate ligands. *Organometallics* **2013**, *32*(3), 885-892. doi:10.1021/om301198b.
23. Martić, G.; Engle, J. T.; Ziegler, C. J. Complexes of 1,3-bis(2-thiazolylimino)isoindoline with middle and late first row transition metals. *Inorganic Chemistry Communications* **2011**, *14*(11), 1749-1752. doi:10.1016/j.inoche.2011.08.001.
24. Payce, E. N.; Knighton, R. C.; Platts, J. A.; Horton, P. N.; Coles, S. J.; Pope, S. J. A. Luminescent Pt(II) complexes using unsymmetrical bis(2-pyridylimino)isoindolate analogues. *Inorganic Chemistry* **2024**, *63*(18), 8273-8285. doi:10.1021/acs.inorgchem.4c00558.
25. Bröring, M.; Kleeberg, C.; Köhler, S. Palladium(II) complexes of unsymmetrical CNN pincer ligands. *Inorganic Chemistry* **2008**, *47*(14), 6404-6412. doi:10.1021/ic800507k.
26. Majerová, S.; Chlupatý, T.; Samsonov, M. A.; Cvačka, J.; Procházková, E.; Růžička, A. Addition of lithium silylamides to 1,2-dicyanobenzene: Isoindoline-1,3-diimine

derivatives investigated by NMR/XRD/DFT approach. *Inorganic Chemistry* **2025**, *64*(15), 7592-7606. doi:10.1021/acs.inorgchem.5c00573.
27. Vlk, L.; Pauk, K.; Samsonov, M. A.; Růžičková, Z.; Chlupatý, T.; Růžička, A. Comprehensive reinvestigation of carbodiimide guanylation: HCl-initiated access to tri- and tetrasubstituted guanidines. *ACS Omega* **2026**, *11*(16), 24075-24085. doi:10.1021/acsomega.5c12436.
28. Dimeji, I. Y.; Abass, K. S.; Audu, N. M.; Ayodeji, A. S. L-Arginine and immune modulation: A pharmacological perspective on inflammation and autoimmune disorders. *European Journal of Pharmacology* **2025**, *997*, 177615. doi:10.1016/j.ejphar.2025.177615.
29. McAllister, R. G. Guanethidine in antihypertensive therapy: Experience with an oral loading regimen. *The Journal of Clinical Pharmacology* **1975**, *15*(11-12), 771-778. doi:10.1002/j.1552-4604.1975.tb02341.x.
30. Hou, F. F.; Boyce, J.; Chertow, G. M.; Kay, J.; Owen, W. F. Aminoguanidine inhibits advanced glycation end products formation on beta2-microglobulin. *Journal of the American Society of Nephrology* **1998**, *9*(2), 277-283. doi:10.1681/asn.v92277.
31. Bailey, C. J. Metformin: Therapeutic profile in the treatment of type 2 diabetes. *Diabetes, Obesity and Metabolism* **2024**, *26*(S3), 3-19. doi:10.1111/dom.15663.
32. Özçeşmeci, M.; Katırcı, R.; Yalçın, M. S.; Özdemir, S. Water-soluble NNN-type pincer ligand and its platinum, copper, and cobalt complexes: Synthesis, characterization, biological activity, and computational docking study. *ACS Omega* **2025**, *10* (40), 46855-46867. https://doi.org/10.1021/acsomega.5c04925.
33. Diana, P.; Martorana, A.; Barraja, P.; Montalbano, A.; Carbone, A.; Cirrincione, G. Nucleophilic substitutions in the isoindole series as a valuable tool to synthesize derivatives with antitumor activity. *Tetrahedron* **2011**, 67(11), 2072–2080. https://doi.org/10.1016/j.tet.2011.01.056.
34. Köse, A.; Bal, Y.; Kishalı, N. H.; Şanlı-Mohamed, G.; Kara, Y. Synthesis and anticancer activity evaluation of new isoindole analogues. *Medicinal Chemistry Research* **2017**, 26(4), 779–786. https://doi.org/10.1007/s00044-017-1793-1.
35. Novotný, M.; Švec, P.; Růžičková, Z.; Růžička, A. Direct access to non-symmetric lithium nitriloamidinate and disymmetric dilithium bisamidinate complexes from 1,3- or 1,4- dicyanobenzene and lithium amides. *Journal of Organometallic Chemistry* **2017**, *849-850*, 88-97. doi:10.1016/j.jorganchem.2017.09.008.
36. Sereda, G.; Rajpara, V. Benzylic oxidation and photooxidation by air in the presence of graphite and cyclohexene. *Tetrahedron Letters* **2007**, *48*(19), 3417-3421. doi:10.1016/j.tetlet.2007.03.072.
37. Russo, L.; Dhar, D.; Backer, R.; Prakash, O.; Matroodi, F.; Overkamp, K.; et al. Direct detection of an NH-π hydrogen bond in an intrinsically disordered peptide. *Nature Communications* **2025**, *16*(1). doi:10.1038/s41467-025-66013-2.
38. Tsuzuki, S.; Honda, K.; Uchimaru, T.; Mikami, M.; Tanabe, K. Origin of the attraction and directionality of the NH/π interaction: Comparison with OH/π and CH/π

interactions. *Journal of the American Chemical Society* **2000**, *122*(46), 11450–11458. https://doi.org/10.1021/ja001901a.
39. Trachsel, M. A.; Ottiger, P.; Frey, H.-M.; Pfaffen, C.; Bihlmeier, A.; Klopper, W.; Leutwyler, S. Modeling the histidine–phenylalanine interaction: The NH···π hydrogen bond of imidazole·benzene. *The Journal of Physical Chemistry B* **2015**, *119* (25), 7778–7790. https://doi.org/10.1021/jp512766r.
40. Becke, A. D. A new mixing of Hartree–Fock and local density-functional theories. *The Journal of Chemical Physics* **1993**, *98*(2), 1372–1377. https://doi.org/10.1063/1.464304.
41. Lee, C.; Yang, W.; Parr, R. G. Development of the Colle–Salvetti correlation-energy formula into a functional of the electron density. *Physical Review B* **1988**, *37*(2), 785–789. https://doi.org/10.1103/physrevb.37.785.
42. Weigend, F.; Ahlrichs, R. Balanced basis sets of split valence, triple zeta valence and quadruple zeta valence quality for H to Rn: Design and assessment of accuracy. *Physical Chemistry Chemical Physics* **2005**, *7*(18), 3297. https://doi.org/10.1039/b508541a.
43. Tomasi, J.; Mennucci, B.; Cammi, R. Quantum mechanical continuum solvation models. *Chemical Reviews* **2005**, *105*(8), 2999–3094. https://doi.org/10.1021/cr9904009.
44. Grimme, S.; Antony, J.; Ehrlich, S.; Krieg, H. A consistent and accurate *ab initio* parametrization of density functional dispersion correction (DFT-D) for the 94 elements H–Pu. *The Journal of Chemical Physics* **2010**, *132*(15). https://doi.org/10.1063/1.3382344.
45. Johnson, E. R.; Keinan, S.; Mori-Sánchez, P.; Contreras-García, J.; Cohen, A. J.; Yang, W. Revealing Noncovalent Interactions. *Journal American Chemical Society* **2010**, 132 (18), 6498–6506. https://doi.org/10.1021/ja100936w
46. Bader, R. F. W. *Atoms in Molecules: A Quantum Theory,* Oxford University Press, 1990.
47. Hansch, C.; Leo, A.; Taft, R. W. A survey of Hammett substituent constants and resonance and field parameters. *Chemical Reviews* **1991**, *91*(2), 165-195. doi:10.1021/cr00002a004.
48. Nelsen, S. F.; Hintz, P. J. Electrochemical oxidation of tertiary amines. Effect of structure upon reversibility. *Journal of the American Chemical Society* **1972**, *94*(20), 7114-7117. doi:10.1021/ja00775a041.
49. Smith, J. R. L.; Masheder, D. Amine oxidation. Part IX. The electrochemical oxidation of some tertiary amines: the effect of structure on reactivity. *Journal of the Chemical Society, Perkin Transactions 2* **1976**, No. 1, 47. doi:10.1039/p29760000047.
50. Mruthunjaya, A. K. V.; Torriero, A. A. J. Mechanistic aspects of the electrochemical oxidation of aliphatic amines and aniline derivatives. *Molecules* **2023**, *28*(2), 471. doi:10.3390/molecules28020471.
51. OECD (2014), Guidance Document on the Validation of (Quantitative) Structure-Activity Relationship [(Q)SAR] Models, OECD Series on Testing and Assessment, No. 69, OECD Publishing, Paris, https://doi.org/10.1787/9789264085442-en.

52. Laskowski, R. A.; Swindells, M. B. LigPlot+: Multiple ligand–protein interaction diagrams for drug discovery. *Journal of Chemical Information and Modeling* **2011**, *51*(10), 2778-2786. doi:10.1021/ci200227u.
53. Vallianatou, T.; Lambrinidis, G.; Tsantili-Kakoulidou, A. In silicoprediction of human serum albumin binding for drug leads. *Expert Opinion on Drug Discovery* **2013**, *8*(5), 583–595. doi:10.1517/17460441.2013.777424.